Turbulence and Internal Waves at the Equator. Part I: Statistics from Towed Thermistors and a Microstructure Profiler

J. N. MOUM, D. HEBERT, C. A. PAULSON, AND D. R. CALDWELL

College of Oceanography, Oregon State University, Corvallis, Oregon

(Manuscript received 18 April 1991, in final form 24 January 1992)

ABSTRACT

High correlations between turbulent dissipation rates and high-wavenumber internal waves and the high values of turbulent dissipation associated with internal wave activity suggest that internal waves are the main direct source of mixing in the thermocline above the core of the Equatorial Undercurrent. An extensive dataset obtained using a microstructure profiler and thermistor chain towed along the equator was analyzed to examine the correspondence between turbulent mixing and high-wavenumber internal waves. In the low Richardson number (Ri) thermocline below the mixed layer but above the core of the Equatorial Undercurrent, and when winds were moderate and steadily westward, it was found that:

- the spectrum of vertical isotherm displacement was dominated by a narrow wavenumber band (corresponding to 150–250-m zonal wavelength) of internal waves;
- both turbulence and internal waves varied diurnally—hourly averaged values of turbulent dissipation rate and wave potential energy were greater by a factor of 100 at night; and
- correlations between turbulent dissipation rate and several measures of internal wave activity (wave isotherm displacement, wave slope, and wave potential energy) were high.

Little or no high wavenumber internal wave activity was observed when winds were light or eastward. Superposing plane waves with the observed characteristics on the observed background field suggests that they are inherently unstable to both advective and shear instability above the core of the Equatorial Undercurrent. These waves are due either to locally generated internal gravity waves or to Kelvin–Helmholz-type instabilities generated in the shear flow; from our measurements these two phenomena could not be distinguished.

1. Introduction

Recent studies of the upper equatorial ocean have revealed that complicated mechanisms are responsible for turbulent mixing (Moum et al. 1989; Gregg et al. 1985; Moum and Caldwell 1985). Turbulence observations made during November 1984 showed that turbulent mixing rates (quantified by the rate of viscous dissipation of turbulent kinetic energy, ϵ) varied with changes in diurnal heating, winds, and proximity to the surface, as well as with other physical processes with time–space scales not resolved by instruments available for that experiment. Above the core of the Equatorial Undercurrent (EUC), there were two mixing regimes, separated vertically. There was a weakly stratified surface layer whose thickness varied 5–35 m diurnally. In this layer, active turbulence was continuous, with daily averages of ϵ varying by only a factor of 2 over a period of 12 days. Between this surface layer and about 85-m depth, turbulence was intermittent. Although the water column was well stratified in this lower layer ($N \sim 0.01$–0.015 s^{-1}), the current shear was sufficient to maintain the gradient Richardson number, Ri, between 1/4 and 1 [$\mathrm{Ri} = N^2/S^2$, where N is the local buoyancy frequency defined by the vertical gradient of density and S is the magnitude of the vertical gradient of horizontal currents. Values of Ri less than 1/4 indicate instability in steady shear flow, whereas higher values indicate stability (Turner 1973, Chapter 4)]. Intermittently occurring turbulence bursts, with lifetimes of 2–3 h, were observed at night and into the early daylight hours. Hourly averages of ϵ were 100 times greater at night than during the day. Daily averages of ϵ varied by a factor of 10 and were highly correlated with the surface wind stress. It was suspected that these thermocline bursts of turbulence were associated with high-frequency internal gravity waves [Gregg et al. 1985; Moum et al. 1989; more recently, McPhaden and Peters (1992) present evidence from moored data at the same site, which indicates a diurnal cycle in the internal wave band of frequencies]. In a flow regime of consistently small Ri, dynamic instability is always imminent; small perturbations can grow rapidly, become unstable, and generate small-scale turbulence. It is conceivable that the additional current

Corresponding author address: Dr. Jim Moum, Oregon State University, College of Oceanography, Oceanography Administration Building 104, Corvallis, OR 97331-5503.

shear induced by internal gravity waves might initiate instability in such a situation by reducing Ri below the critical value of 1/4.

To further examine the correspondence between thermocline bursts and internal waves, we returned to the central equatorial Pacific in the spring of 1987 with the intention of combining our turbulence-profiling measurements with a measure of internal wave activity; this was accomplished by obtaining continuous records of temperature at various depths with a towed thermistor chain. Although background conditions were substantially different from those found in 1984 (Hebert et al. 1991), winds were sufficiently strong and steady for several days to sustain a well-defined diurnal surface layer and a turbulent mixing cycle, as found in 1984. During this period, large-amplitude, narrow wavenumber-band waves were observed below the mixed layer; these occurred intermittently at night and into the early daylight hours but not past noon (§4). In the low Ri thermocline above the core of the EUC, ϵ was positively correlated with the vertical isotherm displacement, wave slope, and potential energy of the dominant waves (§5). An examination of conditions for advective instability and shear instability based on kinematics of plane waves in a shear flow suggests that waves with the observed characteristics are inherently unstable to both mechanisms in the low-Ri equatorial shear flow (§6). We cannot determine whether these waves are internal gravity waves or growing instability waves (see the discussion in §7); for convenience, we will refer to these waves as internal waves in this paper.

2. Experimental details

Measurements were made continually over the period 14–28 April 1987 while traveling eastward along the equator from 140°W to 110°W in the Pacific at an average speed of about 2.5 m s^{-1}. The measurements included vertical microstructure profiles using our Rapid-Sampling Vertical Profiler (RSVP; Caldwell et al. 1985), vertical profiles of currents using the shipboard acoustic Doppler current profiler (ADCP), surface meteorology, and horizontal temperatures using a towed thermistor chain (Spoering 1979). The RSVP, ADCP, and surface meteorology measurements are discussed elsewhere (Hebert et al. 1991). Unique for the purpose of this discussion are the horizontal temperature measurements from the towed thermistor chain (deWitt et al. 1987).

Spacing of thermistors on the chain was nominally 4 m extending from the surface to 125 m. Due to intermittent thermistor failure, some of the nominal depths had missing or no data. For this analysis, data from 25 thermistors obtained during 3000 km of almost continuous towing were analyzed. Sensor depths were determined from a combination of pressure measurements along the chain and a model of chain motion while under tow (Baumann et al. 1982). The accuracy of depth estimates is 0.1 m, and the resolution is 0.01 m. Temperatures were sampled at 20 Hz and averaged over 10 s. This averaging effectively removed fluctuations caused by variations in sensor depths due to surface gravity waves and ship motion. The accuracy of chain temperature measurements is close to 0.01°C, and the resolution is 0.001°C.

The details of the calculations of internal wave statistics, such as rms wave displacement $\langle \zeta \rangle$, are discussed in the Appendix.

3. Background conditions

Surface meteorology conditions at the equator in April 1987 differed considerably from those encountered during our experiments at 0°, 140°W in November 1984. While surface wind stress, τ, was relatively steady in magnitude (mean value $\sim$ 0.1 N m^{-2}) and direction (westward) during November 1984, winds were much weaker and variable in both speed and direction in April 1987. During the first 4-day period (marked at the top of Fig. 1) winds were westward with a mean value of $|\tau| = 0.026$ N m^{-2} (Table 1). Winds shifted to predominantly eastward during period 2 and were much weaker. Although the mean value of $|\tau|$ during period 3 was comparable to that measured during period 1, the direction of the wind stress varied from westward during the first day to weakly eastward for the next 1.5 days, turning to southeastward in the final 1.5 days of period 3 (Fig. 1). Consequently, the mean value of τ_x for period 3 is quite small (Table 1). Several short-lived rain squalls dominated the mean wind stress during this time period (Bahr and Paulson 1991). The average nighttime surface buoyancy flux, J_b^0, estimated from surface heat flux and evaporation was not considerably different among the three periods. However, rainfall associated with squalls encountered during period 3 may result in a considerable additional negative buoyancy flux not considered in the estimates shown in Fig. 1 and Table 1 (Bahr and Paulson 1991); the consequence is a stabilizing influence on the upper ocean.

The mixed-layer depth (MLD; computed as the depth at which σ_t exceeded the surface value by 0.01) ranged from $\sim$5 m during daytimes to maxima of 20 m on two nights, but was more frequently less than 15 m at night (Fig. 1). The nighttime mean value of MLD was largest during period 1. By comparison, our nighttime estimates of MLD from November 1984 (computed using the same definition) were always greater than 20 m and ranged to 35-m depth (Moum et al. 1989). The Monin–Obukhof length scale, L (defined in the caption to Fig. 1), was always less than MLD (excepting a short period near the change in sign of J_b^0 at the end of the night of 27 April) but not substantially so.

The thermistor chain sensor at 28-m depth was positioned at a depth greater than MLD at all times. The

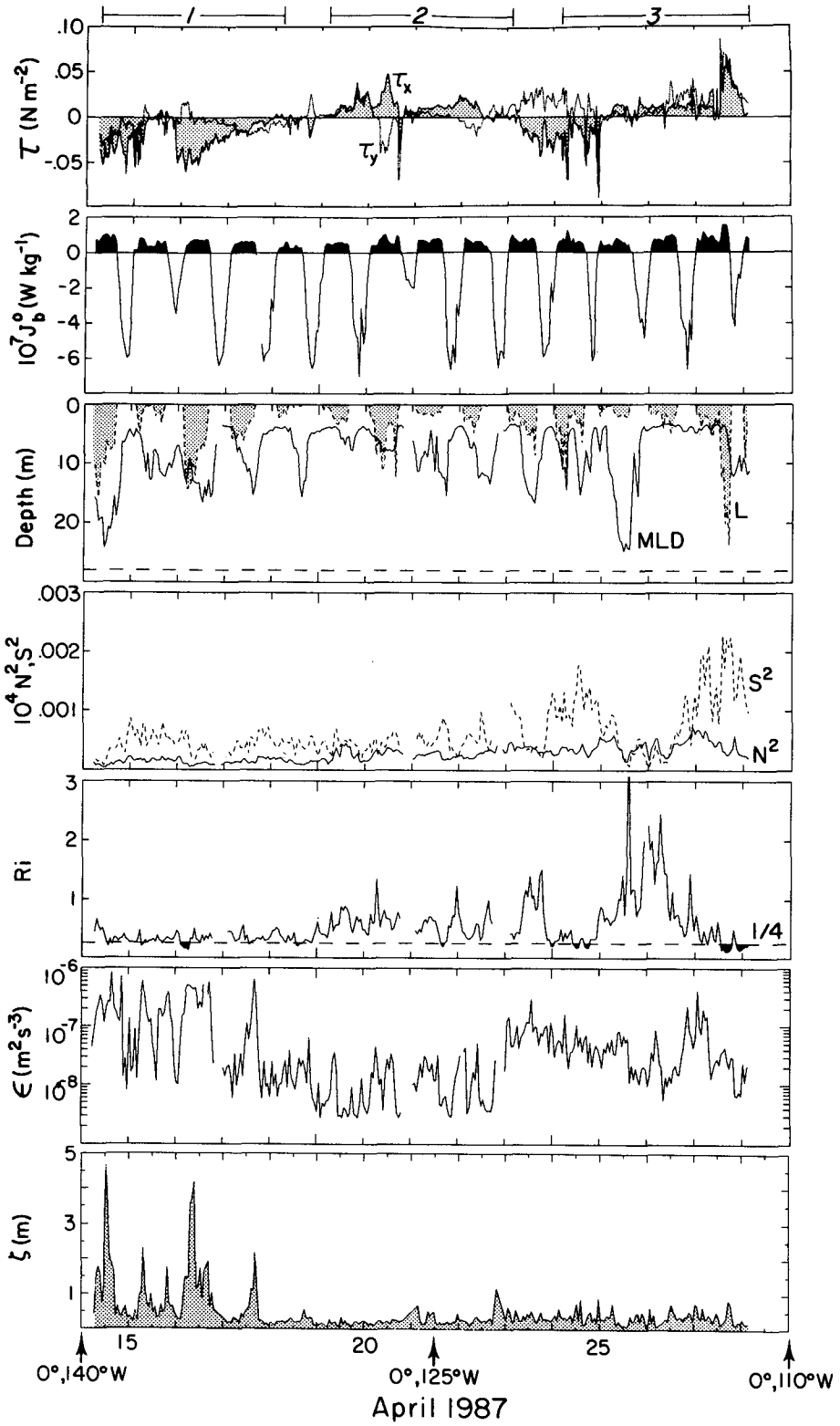

FIG. 1. Hourly averages of: eastward wind stress, τ_x (stippled, $E > 0$); northward wind stress, τ_y (dashed line, $N > 0$); surface buoyancy flux, J_b^0, computed from bulk aerodynamic formulas; mixed-layer depth, MLD, estimated as the depth at which the density exceeds the surface value by 0.01 σ_t units; Monin–Obukhof length scale, $L = -u_*^3/\kappa J_b^0$ ($u_* = (\tau/\rho)^{1/2}$, $\kappa = 0.4$); squared shear magnitude, S^2; squared buoyancy frequency, N^2; Richardson number, Ri; turbulent dissipation, ϵ; and rms wave displacement, ζ, at 28-m depth. The measurements were made while transiting along the equator between 140°W and 110°W in April 1987 (locations marked at bottom of plot). For further analysis, the data were subdivided into three periods, each approximately 4 days long, chosen to begin and end at the same local times. They correspond to the following periods (UTC) and locations: (Period 1) 0530 14 April, 139°56′W to 0330 18 April, 132°19′W; (Period 2) 0430 19 April, 130°03′W to 0230 23 April, 121°14′W; (Period 3) 0330 24 April, 118°47′W to 0130 28 April, 110°14′W.

TABLE 1. Average daytime and nighttime values of the parameters shown in Fig. 1 for each of the three periods of our equatorial transect; $|\tau|$ represents the magnitude of the wind stress; τ_x ($E > 0$) and τ_y ($N > 0$) are vector components.

	Period 1		Period 2		Period 3	
	Day	Night	Day	Night	Day	Night
$\|\tau\|$ (N m^{-2})	0.026	0.025	0.015	0.017	0.022	0.025
τ_x (N m^{-2})	−0.023	−0.020	0.011	0.011	0.0019	0.0049
τ_y (N m^{-2})	−0.0050	−0.0092	0.0048	0.00079	0.0077	0.015
$10^7 J_b^0$ (W kg^{-1})	−2.2	0.64	−1.7	0.59	−0.44	0.69
MLD (m)	5.6	12.1	4.9	7.4	5.8	8.7
L (m)	—	−6.2	—	−3.1	—	−4.5
$10^4 N^2$ (s^{-2})	1.6	1.3	2.4	2.8	4.5	3.8
$10^4 S^2$ (s^{-2})	5.2	4.2	4.2	5.1	9.1	9.4
Ri	0.34	0.33	0.59	0.59	0.99	0.69
$10^8 \epsilon$ (W kg^{-1})	4.0	22.	2.5	1.3	5.1	4.7

remaining panels in Fig. 1 represent hourly averages at 28-m depth. During period 1, Ri was consistently small (sometimes <1/4 in hourly means); nighttime and daytime values were equal. Generally ϵ, was large only at night and into the morning hours, followed by daytime suppression of turbulence: a scenario similar to that observed in November 1984 (Moum et al. 1989; Peters et al. 1988). High-frequency internal wave activity (as depicted by wave isotherm displacement ζ; discussed in more detail in the next section) was observed only during period 1 and was confined to nighttime or early morning hours. This period was the only

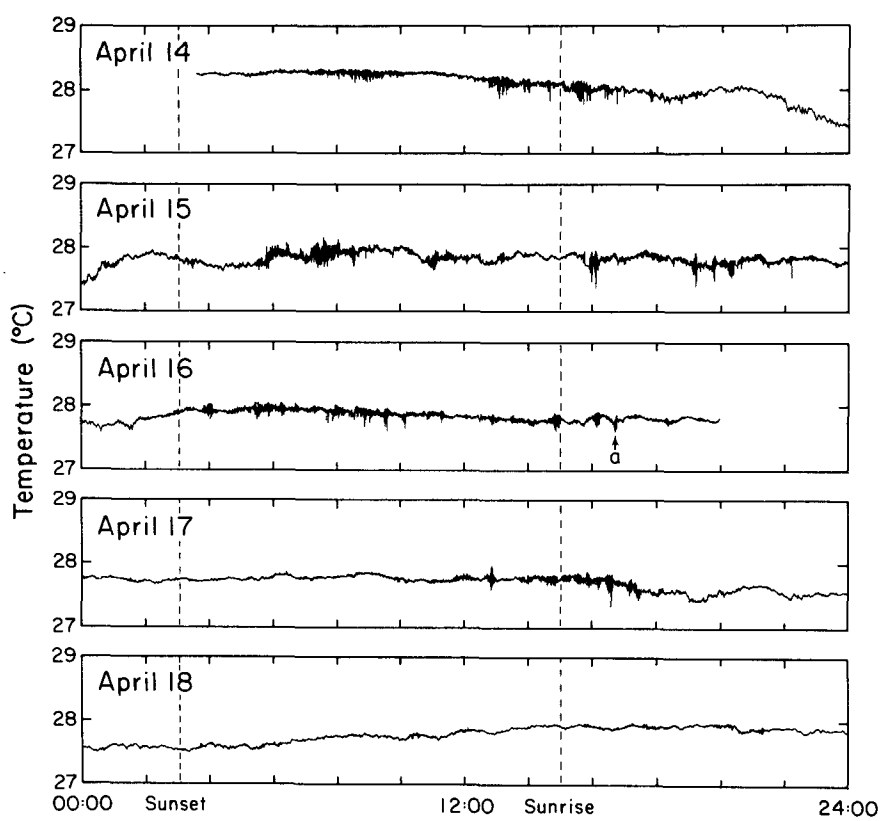

FIG. 2. Five-day record of temperature along the equator from a thermistor at 28-m depth. Each panel represents one full day between 0000 and 2400 UTC. Longitudes were 140°04'W at 0341 14 April at the beginning of the transect; 138°28'W at 0000 15 April; 136°29'W at 0000 16 April; 134°42'W at 0000 17 April; 132°39'W at 0000 18 April. Sunrise was approximately 0600 local time (~1500 UTC) and sunset was 1800 local (~0300 UTC). The event denoted *a* on 16 April was a particularly energetic, though short-lived, patch through which a single RSVP profile was obtained and is the focus of the analysis of Hebert et al. 1992.

one during which moderate, westward winds were sustained and Ri was consistently small.

4. Properties and variability of the internal wave field

The most remarkable feature in a long record from an individual thermistor is the intermittency of the high-frequency component of the signal (Fig. 2). During the first 4 days of the record, patches of high-frequency signal appeared intermittently and were concentrated in the time period following sunset until several hours past sunrise. The duration of the patches ranged from several minutes to many hours (corresponding to several hundreds of meters to several tens of kilometers in the zonal direction). The amplitude of the high-frequency temperature signal ranged from 0.1° to 0.3°C. By the fifth day, the high-frequency component of the temperature variance was weak, and for the remainder of the experiment's 14 days there was little or no high-frequency signal in the record.

Spectra of vertical displacement computed for segments of the thermistor record at 28 m (of which Fig. 2 is a subset) illustrate two important results (Fig. 3). First, there is a band of frequencies for which the nighttime-averaged spectrum for the first 4 days was significantly higher than that for any of the other periods (day or night). The daytime-averaged spectrum for the first 4 days (Fig. 3, left panel) was approximately equivalent to that for the other two nighttime and daytime periods. For the remainder of the period, there was no significant difference between day and night spectra (Fig. 3, middle and right panels). Second, the energy was apparently confined to a narrow band of frequencies with a peak at about 0.01 Hz, or slightly higher. Although frequency spectra were computed from our time series, we really consider the data to be a spatial series since the buoyancy period at this depth (~600 s) is long compared to the period of the narrowband peak (50–100 s). The simple frequency-to-wavenumber conversion using the ship speed, U, that is, $k = 2\pi f/U$, shows that the apparent zonal wavelength of the spectral peak is ~150–250 m (the wavelengths shown at the tops of Figs. 3a, 4 were derived in this manner).

Coherence between the thermistor at 28 m and those both above and below showed the signal of the narrowband peak in the frequency spectrum to be vertically coherent over all of the sensors below 28 m for the first 4 days of the experiment (Fig. 4). For frequencies less than 0.006 Hz (horizontal scales greater than 400 m), the squared coherence dropped below 0.1 (which represents 99.999% significance) for vertical separations greater than 25 m. At frequencies greater than 0.03 Hz (horizontal scales smaller than 80 m), the corresponding vertical coherence scale was closer to 5 m (or one sensor spacing). By comparison, the squared coherence was greater than 0.3 at 0.01 Hz over the observed depth range below 28 m. Above 28 m the

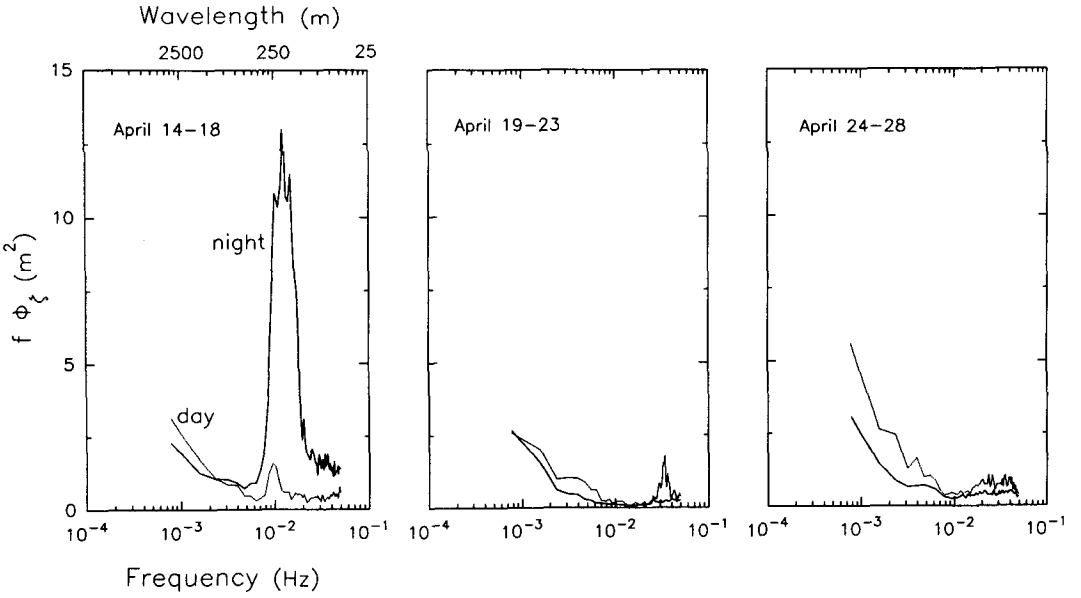

FIG. 3. Variance-preserving displacement spectra computed from the temperature record at 28 m divided by the mean vertical temperature gradient. The data were subdivided into days (2100–0400 UTC) and nights (0400–2100 UTC). The unequal subdivisions were chosen to ensure inclusion of the late morning events in the nighttime data. The 512-point segments were windowed (10% cosine) and detrended. Spectra were computed and bin averaged. Each panel represents averaged spectra from 4 days/nights corresponding to the periods denoted in Fig. 1; the leftmost panel represents period 1. Horizontal wavelength corresponding to a mean ship speed of 2.5 m s^{-1} is indicated at the top of the first panel. Daytime spectra have 112 degrees of freedom and are represented by dotted lines. Nighttime spectra have 248 degrees of freedom and are represented by solid lines.

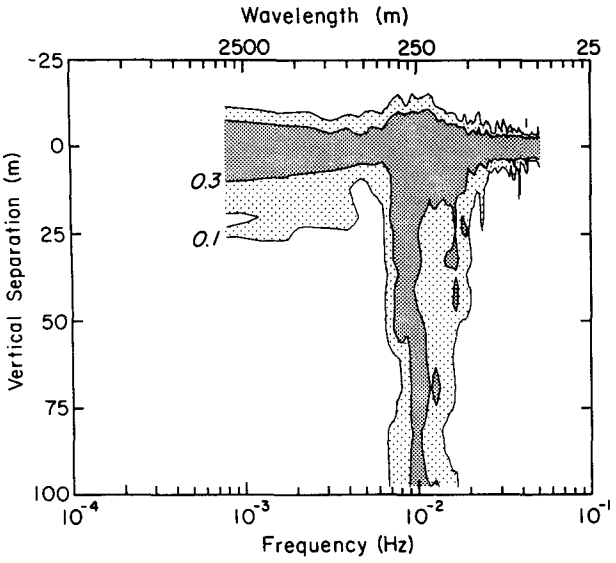

FIG. 4. Vertical separation-frequency contours of squared coherence for the nighttime data from the first 4-day interval (Fig. 3, first panel). These represent the coherence between the thermistor at 28 m (Fig. 2) and those both above and below. With 248 degrees of freedom, a value of squared coherence equal to 0.1 is significantly different from 0 at more than a 99.999% level of significance. Outside the shaded region the squared coherence drops rapidly to a value that is not significantly different from 0 at the 95% confidence level. The coherence is significant over the narrowband peak in the nighttime displacement spectrum of Fig. 3 (first panel) for all depths below 28 m and to the deepest sensor at 125 m. At the shallowest depths, the temperature signal due to waves was weak. Corresponding wavelengths are shown at the top of the figure.

frequently weak stratification resulted in weak wave signals and hence, low coherence, even at 0.01 Hz. The high vertical coherence at 0.01 Hz is strong evidence for the wavelike nature of the narrowband signal in the records during the first 4 days of our experiment. Our estimate of T', from which wave statistics were estimated (see the Appendix), is dominated by this narrowband signal.

Some aspects of the structure of the waves can be deduced from the relative phase dependence on depth and horizontal temperature gradient skewness (third moment of the distributions of dT/dx) estimates. The record from the first 4 days shows a significant vertical phase dependence at the frequency of the narrowband peak (Fig. 5). Where the shear magnitude was maximum, between 12- and 40-m depth, there was a change in phase of 90°, with the signal nearest the surface leading; that is, the waves appeared to be shifted towards the surface in the direction of the mean currents (and the direction of surface winds). This phase shift can be seen in individual wave packets [e.g., Fig. 3a from Hebert et al. (1992); hereafter referred to as Part II]. The skewness of dT/dx was determined for all of the chain thermistors; it was significantly different from zero and was positive in the depth range where the phase exhibited depth dependence (above 40 m; Fig. 5). Positive skewness implies that the temperature fronts were steeper on the westward sides of the waves than on the eastward sides. Not only were the waves shifted westward towards the surface, they were also tilted westward.

During the first 4 days the isotherm displacement variance in the narrow, high-frequency band was greater by nearly a factor of 10 at night compared to that found during days (Fig. 3). For the remainder of the record, the narrowband signal was nonexistent. This is illustrated by the change in distributions of hourly rms values of isotherm displacement, $\langle \zeta \rangle$, and wave potential energy, $N^2\langle \zeta^2 \rangle$, between the first 4 days and the last 10 days of the experiment (Fig. 6). While the last 10 days were characterized by the large number of estimates of $\langle \zeta \rangle$ at or near the noise level of the calculation (50% were smaller than 0.25 m), only 17% fell in this category during the first 4 days. Although the ratio of mean values of $\langle \zeta \rangle$ for the two periods was $\sim$2.6, the ratio of $N^2\langle \zeta^2 \rangle$ did not change in proportion to the square of the ratio of $\langle \zeta \rangle$ because N^2 was correspondingly larger farther eastward during the last 10 days of the experiment (Fig. 1).

The day to night variability as a function of depth is clear in vertical profiles from the first 4 days of the experiment (Fig. 7). Nighttime mean values of ϵ were 5 to 10 times greater than daytime values in the low-Ri zone above the EUC core (Hebert et al. 1991), as we found in November 1984 (Moum et al. 1989). Below 50 m, Ri increased rapidly, and there was no significant day–night difference in ϵ. Below the EUC core, N^2 was small, but the shear was not large enough to reduce Ri much below 1; Ri was 2 to 4 times larger than above the EUC core. Mean values of ϵ were small below the EUC core. Nighttime values of displacement, $\langle \zeta \rangle$, and wave slope, $\langle \zeta_x \rangle$, were greater than daytime values above 50 m but not below. Since the displacements were dominated by a narrow band of wavelengths, $\langle \zeta \rangle$ and $\langle \zeta_x \rangle$ are highly correlated. That is, changes in $\langle \zeta_x \rangle$ were due primarily to changes in ζ rather than to changes in horizontal wavenumber; to demonstrate, the average wave slope for displacement ζ is obtained by dividing the maximum value of ζ by one-quarter wavelength. For a dominant wavelength of 150 m, a 1-m displacement corresponds to $\langle \zeta_x \rangle \sim 0.03$, as can be seen in Fig. 7. Nighttime values of $N^2\langle \zeta^2 \rangle$ were large both above and below the EUC core. The large, deep values of wave energy were mainly due to higher values of N^2, not $\langle \zeta \rangle$, below the EUC core.

5. Correlation of ϵ and internal wave statistics

A qualitative comparison between ϵ and the thermistor record shows the tendency for ϵ to increase during periods of high-frequency activity in the temperature record (Fig. 8), at least during the first 4 days of the experiment. For example, starting at about 0700 UTC

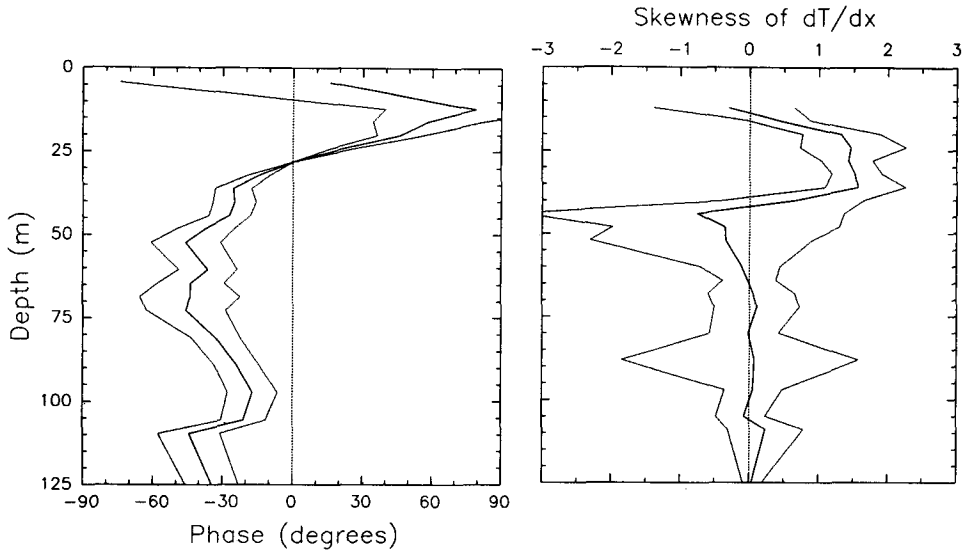

FIG. 5. Left panel: vertical profile of phase relative to the thermistor at 28 m at a frequency of 0.01 Hz, corresponding to the peak in coherence in Fig. 4. The signal at 50 m lags the signal at 15 m by ~90°. The 95% confidence intervals were computed using the form given by Jenkins and Watts (1968, p. 380). Right panel: Vertical profile of the skewness of horizontal temperature gradients, dT/dx computed for the nighttime data of the first 4-day period. The 95% confidence intervals were computed using the bootstrap method.

15 April (or ~4 hours past sunset) a large increase in high-frequency wave activity appeared in the thermistor record. The corresponding increase in ϵ was sustained over the duration of the patch (~3 hours), decreasing to a minimum by 1400 UTC, followed by an increase coincident with several shorter, energetic bursts. This record contrasts with the events of 17 April, during which high-frequency waves did not appear until almost 1200 UTC (or 9 hours past sunset); ϵ remained low until the wave activity increased, stayed high coincident with the energetic waves, and decreased by 2½ orders of magnitude between 1630 and 1930 (during the early daylight hours) when the high-frequency waves virtually disappeared from the thermistor record for the remainder of the experiment. The mean value of ϵ over the depth range 16–36 m was almost four times smaller during the last 10 days than in the first 4 days (Fig. 6).

The correlation was high between $\log\epsilon$ and $\log N^2\langle\zeta^2\rangle$ over the depth range 16–36 m. At 28-m depth, the sample correlation coefficient was 0.83 (Fig. 9); with 90 data points, a correlation of 0.26 is significantly different from zero at the 95% confidence level. Although on average $N^2\langle\zeta^2\rangle$ was as high below 40 m as above (Fig. 7), ϵ was not correspondingly large, and hence, correlations were low. Basically, the correlations were significant only in the low-Ri thermocline above the EUC core (Fig. 10). Correlating the $N^2\langle\zeta^2\rangle$ estimates from all six thermistors in the depth range 16–36 m with the corresponding ϵ estimates (506 data points) yields a correlation coefficient 0.78, not significantly different from that obtained using only the thermistor at 28 m. Below 36 m, the correlation decreased with depth and is not significant below 50 m, with the exception of a puzzling point at 95-m depth.

Although it may be more intuitively pleasing to correlate wave energy ($N^2\zeta^2$) to rate of change of energy (ϵ), there is really no indication from our computations that the turbulence is correlated to any parameter other than simply the presence of the waves. Over the depth range 16–36 m, there was no difference between the correlation of $\log\epsilon$ with $\log N^2\langle\zeta^2\rangle$ ($r = 0.78$), $\log\langle\zeta\rangle$ ($r = 0.78$), or $\log\langle\zeta_x\rangle$ ($r = 0.81$). Variations in N^2 in this depth range were apparently too small to affect the correlation with $N^2\langle\zeta^2\rangle$. Since the signal was confined to such a narrow band of scales (Fig. 3), variations in $\langle\zeta_x\rangle$ were largely due to variations in ζ rather than to any change in horizontal wavelength of the energetic waves; this is reflected in the fact that the correlations do not differ with wave parameters.

We note that our statistical comparison is somewhat affected by our averaging. For cases in which the high-frequency turbulence bursts were less than 1 h in duration (which is equivalent to about 9 km along the equator), we have attenuated both rms wave statistics and ϵ by averaging over 1 hour. Although the towed thermistor record is continuous over the period, the profiler estimates of ϵ are discrete. The natural intermittency of the turbulent flow was not well resolved in time or space. For example, only a single RSVP profile was made through the wave packet encountered at 1600 UTC 16 April (part II: denoted by a in Fig. 2). This example emphasizes the lack of an exact 1-to-1 correspondence in the statistics. Although the sig-

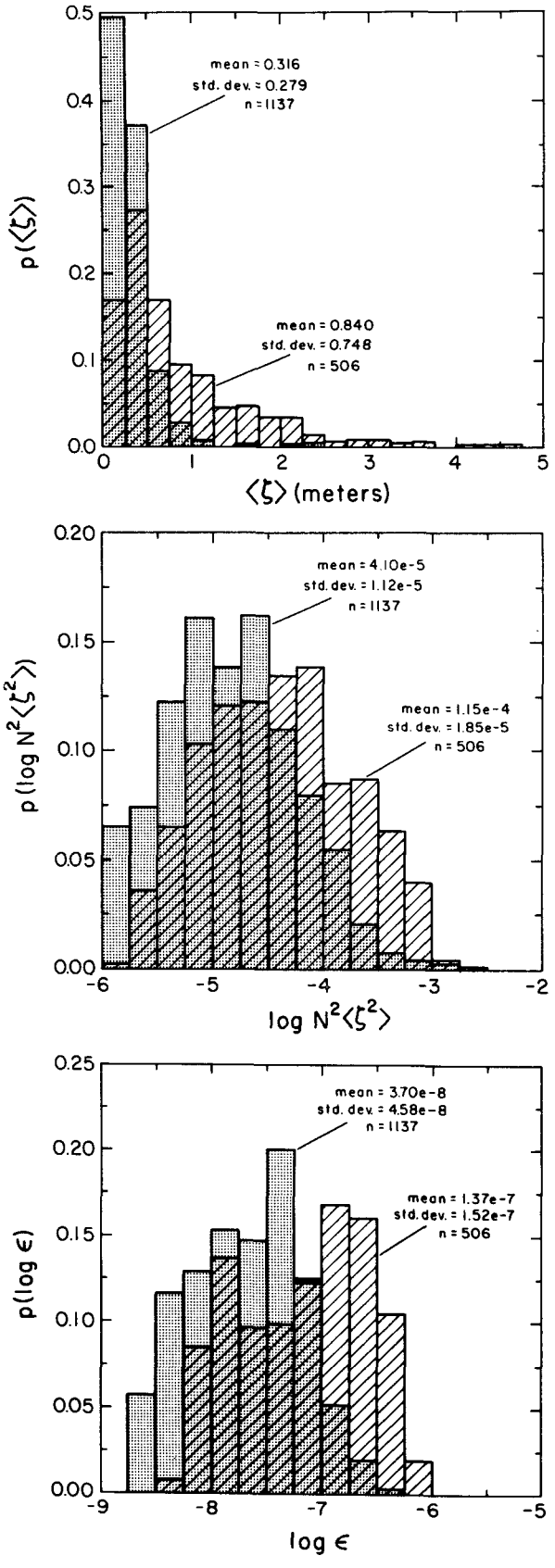

nature of the waves was strong from the surface to 125 m, the single profile showed ϵ to be high only between 45 and 70 m. In this case, the effect of the wave is represented in the histogram of Fig. 6, which covers the depth range 16–36 m, but the corresponding mixing is not, since it occurs below this depth range. Given the limitations in the sampling, the correlations are surprisingly good.

6. Kinematic estimates of internal wave stability

As we suspected based on our 1984 observations, thermocline bursts of high ϵ were closely related to these intermittent packets of internal waves. Correlations between ϵ and any reasonable parameter computed from ζ are high. Unfortunately, this limits our insight into the mechanics of instability. Since ϵ is no more closely related to wave slope, $\langle \zeta_x \rangle$, than any other wave parameter, for example, the relative importance of advective instability cannot be evaluated as the decay mechanism for the internal waves from our statistical analysis. Instead, our approach is to superpose the structure of a linear plane wave with observed or reasonable properties on the background field and then to assess the propensity for advective instability (for which the velocity of a water parcel exceeds the phase speed of the wave) and shear instability (for which the local value of Ri diminishes below 1/4).

Consider a linear plane wave with frequency ω and zonal wavenumber k traveling along the equator (x direction) with instantaneous vertical displacement

$$\zeta = Z(z)e^{i(kx-\omega t)} \tag{1}$$

and wave horizontal velocity

$$u = U(z)e^{i(kx-\omega t)}, \tag{2}$$

where U, Z are depth-dependent functions with amplitude and phase. The vertical velocity is given by the linearized form (neglecting the nonlinear wave term $u\zeta_x$ but retaining the interaction of the mean velocity with the wave)

$$w = \frac{D\zeta}{Dt} = \zeta_t + \bar{u}\zeta_x = -i\omega\zeta + i\bar{u}k\zeta. \tag{3}$$

The mean zonal current velocity, $\bar{u}$, is depth dependent. For zonally propagating plane waves, only the zonal component of mean current velocity contributes to the advective component of w. From continuity

$$w_z = -u_x = -iku = -i\omega\zeta_z + ik(\bar{u}_z\zeta + \bar{u}\zeta_z). \tag{4}$$

FIG. 6. Histograms of $\langle \zeta \rangle$, $N^2\langle \zeta^2 \rangle$, and ϵ for thermistors located in the depth range 16–36 m. Hatched areas represent the first 4 days of the equatorial transect while stippled bars represent the last 10 days. Arithmetic mean values and standard deviations are shown in the figures.

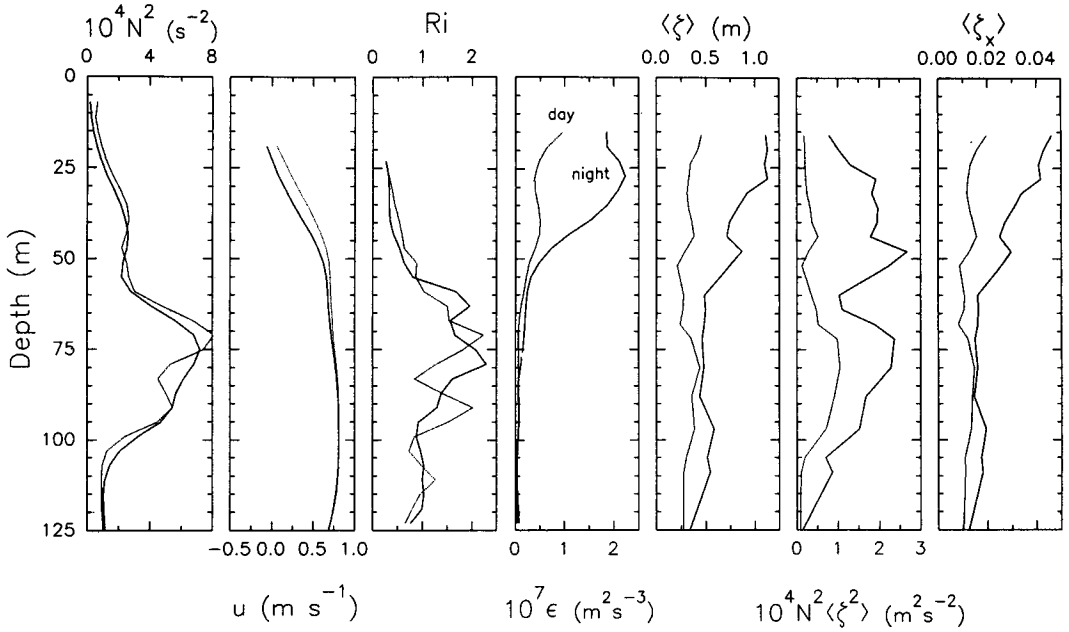

FIG. 7. Vertical profiles of N^2, $\bar{u}$, Ri, ϵ, $\langle\zeta\rangle$, $N^2\langle\zeta^2\rangle$, and $\langle\zeta_x\rangle$ averaged over daytime and nighttime intervals defined in the caption to Fig. 3 for the first 4-day interval of the equatorial transect. Nighttime averages are represented by solid lines and daytime averages by dotted lines.

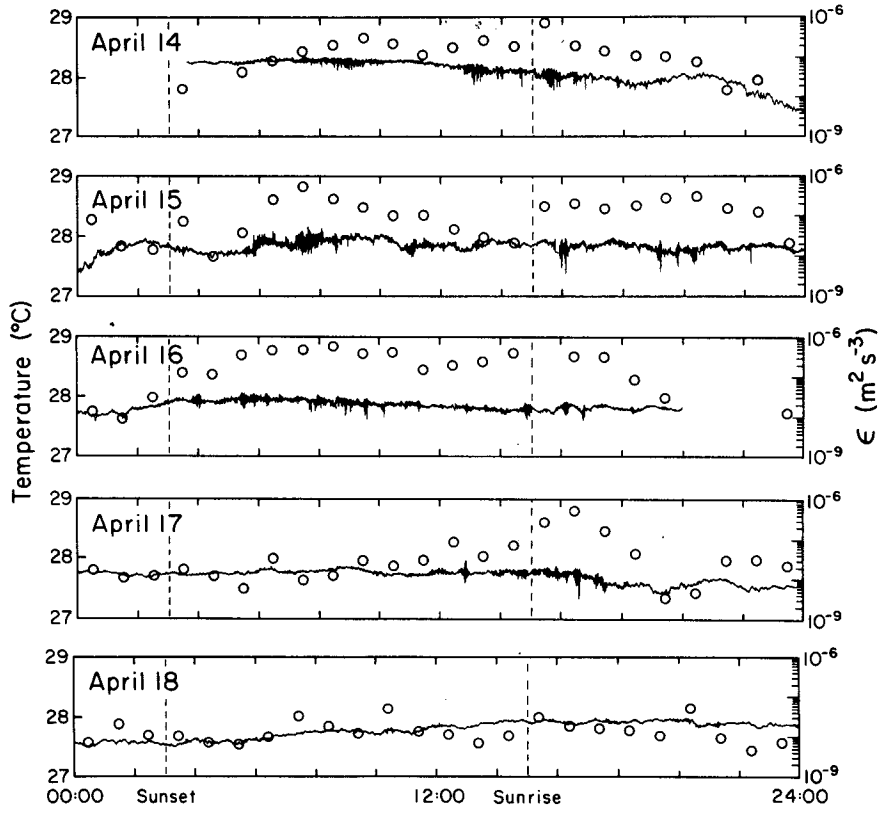

FIG. 8. Hourly averages of ϵ, vertically averaged over $\pm$ 5 m about the thermistor at 28 m, plotted as a time series to correspond to the temperature record of Fig. 2.

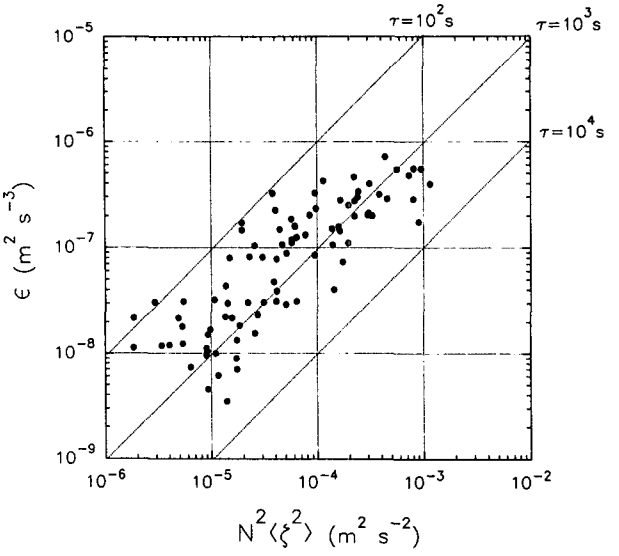

FIG. 9. Plot of ϵ versus $N^2\langle\zeta^2\rangle$ for the thermistor at 28-m depth over the first 4-day interval defined in the caption to Fig. 1. The sample correlation coefficient is 0.83. With 90 data pairs, a value of 0.26 is significantly different from 0 with 95% confidence. Dashed lines with a slope of one indicate constant decay time scales of internal wave energy by turbulence, denoted by $\tau = N^2\langle\zeta^2\rangle/\epsilon$.

Therefore,

$$u = (c - \bar{u})\zeta_z - \bar{u}_z\zeta \tag{5}$$

and

$$u_z = (c - \bar{u})\zeta_{zz} - 2\bar{u}_z\zeta_z - \bar{u}_{zz}\zeta, \tag{6}$$

where $c = \omega/k$ is the zonal component of the phase speed.

The condition for advective instability, for which the local particle speed exceeds the phase speed of the wave, can be written as

$$\frac{u}{c} = \left(1 - \frac{\bar{u}}{c}\right)\zeta_z - \bar{u}_z\frac{\zeta}{c} > 1. \tag{7}$$

Shear instability is governed by the local instantaneous value of the gradient Richardson number. The shear instability condition due to the presence of the wave in a sheared flow is given by

$$\mathrm{Ri}_o = \frac{N^2}{(u_z + \bar{u}_z)^2}$$

$$= \frac{N^2}{[(c - \bar{u})\zeta_{zz} - 2\bar{u}_z\zeta_z - \bar{u}_{zz}\zeta + \bar{u}_z]^2} < \frac{1}{4}. \tag{8}$$

To obtain estimates for the quantities u/c and Ri_o, values for $\bar{u}$, $\bar{u}_z$, c, ζ, ζ_z, and ζ_{zz} must be determined. The first two parameters are mean quantities that can be obtained from Fig. 7. We can estimate the phase speed from our measure of zonal wavelength (Fig. 3) and from assuming that the frequency of the internal waves is near the local buoyancy frequency (McPhaden and Peters 1992). Estimates of ζ, ζ_z, ζ_{zz} were made from the towed thermistor data for periods of particularly energetic internal wave activity.

Since neither the magnitude nor direction of the phase speed of these waves is known, we examined the conditions (7) and (8) for a wide range of c. However, realistic bounds on c can be established from our data. Since we cannot determine wave frequency, ω, from our data, we refer to McPhaden and Peters (1992), who have identified a high-frequency peak in temperature spectra from moored measurements at 0°, 140°W. They interpret this peak to be due to the same phenomenon (internal gravity waves or Kelvin–Helmholz instability waves) that caused the peak in our spatial series of isotherm displacements (Fig. 3). The spectral peak from the time series was found at frequencies much greater than the local buoyancy frequency. McPhaden and Peters assumed this to be due largely to Doppler shifting of the wave signal relative to the EUC and that the inherent wave frequency is actually near N for waves with vertical wavenumber approximately equal to or smaller than the horizontal wavenumber [see McPhaden and Peters' Eq. (1)]. Since our vertical coherence estimates are large and phase estimates are zero below 40 m, it seems that the vertical scale of the waves is at least as great as the length of our thermistor chain, which is approximately the wavelength associated with the spectral peak of Fig. 3. For our purposes, then, it seems reasonable that ω is not different from N by more than a factor of 2. With $\omega \sim N/2$, our estimate of phase speed is $c = \omega/k \sim \lambda N/4\pi$. With our zonal wavelength estimate of ~200 m and $N \sim 0.01$ s^{-1} (typical of the depth range 15–40

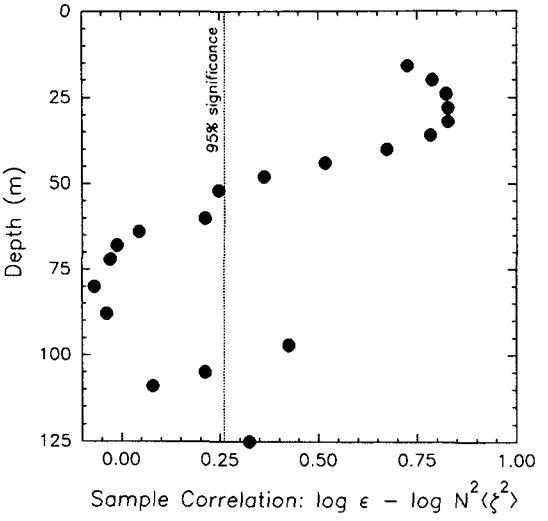

FIG. 10. Vertical profiles of sample correlation coefficients between ϵ and $N^2\langle\zeta^2\rangle$ estimated for all thermistors for the first 4-day interval. Correlations above 0.26 are significantly different from 0 at the 95% confidence level. The correlation is systematically significant only above 50 m.

m; Fig. 7), $c \sim 0.16$ m s^{-1}, while $c \sim 0.04$ m s^{-1} with $N \sim 0.005$ s^{-1} and $\lambda \sim 100$ m. The upper bounds to these estimates ($c \approx 0.2$–0.3 m s^{-1}) occur when $\omega = N$. We expect $c \sim 0.1$ m s^{-1} to be a reasonable estimate for the magnitude of the phase speed, although there remains an ambiguity in the sign of c (eastward- or westward-propagating waves). (While for this analysis only zonally propagating waves are considered, we note that in absolute terms this wavelength estimate must be considered an upper bound since any unresolved meridional component will reduce the wavelength further. Hence, while our estimate of c represents the zonal component of phase speed, it is an upper bound to the absolute phase speed.)

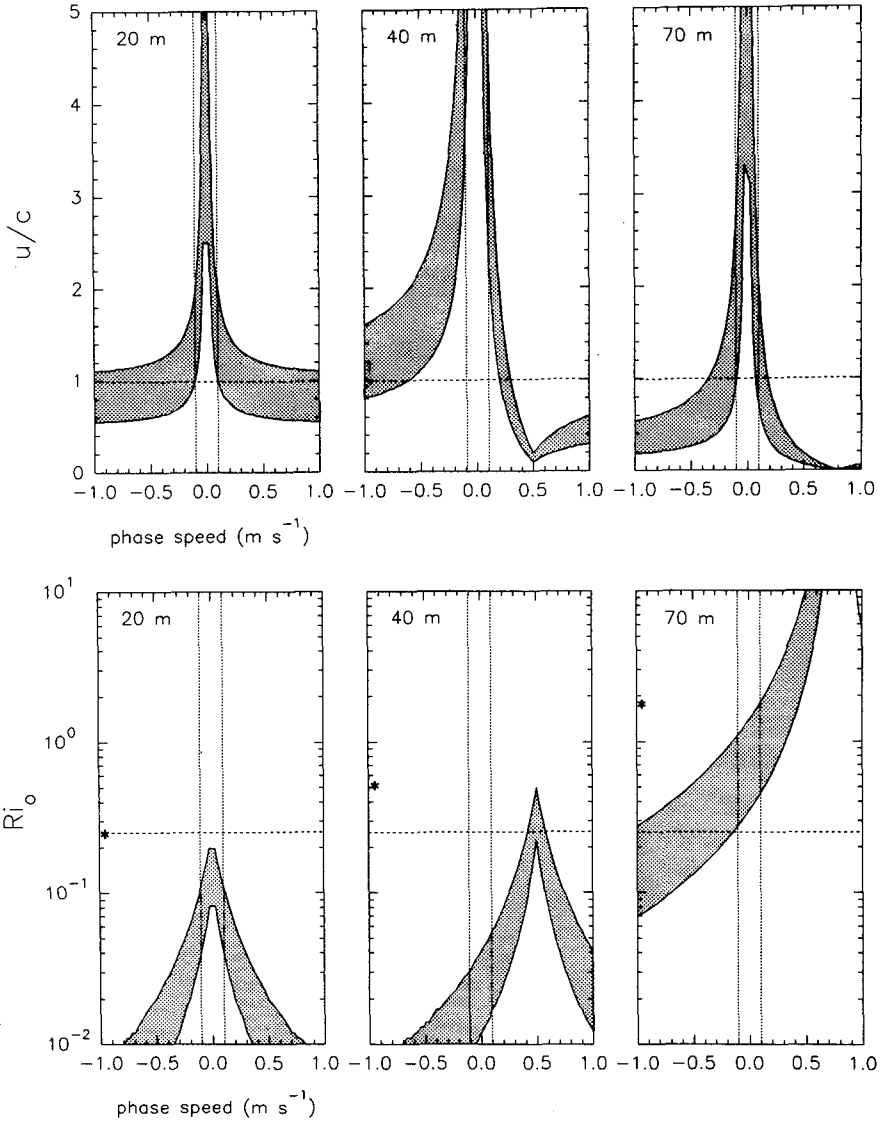

FIG. 11. Upper panel: ratio of maximum possible particle velocity to phase speed as a function of phase speed according to Eq. (7). Because the phase relations between ζ, ζ_z, and ζ_{zz} cannot be determined, the sign of each of the terms in (7) are uncertain. The maximum value of u as $u = |(c - \bar{u})\zeta_z| + |-\zeta\bar{u}_z|$ is estimated. The computation was done at three different depths. The values for the parameters used are listed in Table 2 and discussed in the text. The horizontal line at $u/c = 1$ indicates the condition for advective instability. Vertical lines indicate $c = \pm 0.1$ m s^{-1}. Lower panel: Richardson number, $\mathrm{Ri}_o = N^2/(u_z + \overline{u_z})^2$, computed from Eq. (8) and the data in Table 2. For the reasons stated above, u_z was estimated from $u_z = |(c - \bar{u})\zeta_{zz}| + |-2\zeta_z\bar{u}_z| + |-\zeta\bar{u}_{zz}|$. The horizontal line indicates Ri = 1/4. Vertical lines indicate $c = \pm 0.1$ m s^{-1}. Stars at the left-hand side of each panel indicate the mean value of background Ri at each depth. For the computation of Ri_o at 70-m depth, $\overline{u_z} = 0.0$ was chosen; as a result, Ri_o exceeds the averaged background value of Ri as $c \to \bar{u}$.

Although the computation of ζ, ζ_z, ζ_{zz} from the thermistor chain data is noisy, we have made rough estimates in two ways. Since our interest is in the effects of energetic waves, we have computed rms estimates during short periods of intense wave activity (20 min–1 h). During these periods, we estimated the threshold values above which 5% of the values were found. Over short periods of energetic wave activity, estimates of both $\langle \zeta_z \rangle$ and $\langle \zeta_{zz} \rangle$ in the depth range 10–50 m were considerably higher when high-frequency waves were present than when they were not present. For example, during a reasonably energetic 25-minute period on 17 April from 1620 to 1645 UTC (Fig. 2), the rms value of $\langle \zeta_{zz} \rangle$ was ~ 0.1 m^{-1} above 50 m (and 5% of the 10-second estimates from this period were >0.2 m^{-1}) but much smaller below 50 m. Over other similar energetic periods this appears to be a reasonable range of $\langle \zeta_{zz} \rangle$ produced by the presence of the internal waves. Corresponding values of $\langle \zeta_z \rangle$ were about 0.4 (5% > 0.8). Also, in Part II we calculated *instantaneous* estimates from the thermistor chain data for the wave packet examined in detail (see Fig. 3 of part II). These estimates agree fairly well with the rms estimates.

The conditions (7) and (8) were evaluated as functions of c using the data estimates of parameters; results are summarized in Fig. 11. A summary of the data estimates is presented in Table 2. Estimates of wave parameters were made at three depths: 20 m (where $\bar{u} = 0$); 40 m (within the range of peak correlation between wave activity and turbulent dissipation); and 70 m (in the high-Ri region). In each case, $\bar{u}_{zz} \approx 0$; even at depths where $\bar{u}_{zz} \neq 0$, this term makes only a small contribution to the wave shear based on (6). Mean values of N^2, $\bar{u}$, and $\bar{u}_z$ and our conservative estimates of maxima for each of ζ, ζ_z, ζ_{zz} at each depth are listed in Table 2. Since we are unsure of both magnitude and direction of c, we computed u/c and Ri_o for a range of c; however, based on our previous argument, the magnitude is not expected to differ greatly from 0.1 m s^{-1} (say 0.05–0.2 m s^{-1}). For the reader's guidance, vertical dashed lines in each panel of Fig. 11 represent $c = \pm 0.1$ m s^{-1}.

First, consider the behavior of the advective stability parameter, u/c. Increasingly larger values of u/c (>1) suggest an increased likelihood that the waves may be advectively unstable. Slow-moving waves are more prone to advective instability than are fast-moving waves. The depth-increasing asymmetry in the curves at 40 and 70 m is due to the depth-increasing eastward velocity between those depths. As a result, below the depth of zero mean zonal velocity, westward-propagating waves (those traveling opposite to the mean flow) are more likely to be advectively unstable than eastward-propagating waves. Because ζ_z and ζ_{zz} are substantially smaller at 70 m than above this depth, the band of phase speeds with high values of u/c is more narrowly confined to small values of c.

Now consider the behavior of the shear instability parameter, Ri_o. Decreasing values of Ri_o ($<1/4$) suggest an increased likelihood of shear instability. In contrast to the conditions for advective instability, fast-moving waves (those whose phase speeds differ substantially from $\bar{u}$) are more prone to shear instability than slow-moving waves. Again, the asymmetry is due to the depth-varying eastward velocity. A maximum occurs where $c = \bar{u}$. As a result, below 20 m, waves propagating westward exhibit smaller values of Ri_o and hence are more likely to be unstable than eastward-propagating waves. At 70-m depth, the increased stratification results in a much higher value of Ri_o.

To summarize the result depicted in Fig. 11, there seems to be a depth range in the low-Ri zone above the EUC core where internal waves with a wide range of phase speeds (a range that includes our estimate of the most probable values of c) are inherently unstable. Because both instability criteria are satisfied over a large range of c, given our wave parameters, it is impossible to say whether advective or shear instability is the primary mechanism for generating the observed ϵ.

In the preceding discussion, we have ignored the influence of wave strain on the local buoyancy frequency and, hence, Ri. The relative vertical motion of isopycnal surfaces (the wave strain, ζ_z) acts to change the stratification according to

$$N^2 = \frac{-g}{\rho} \frac{\delta\rho}{(\delta z + \zeta_z \delta z)} = \frac{-g}{\rho} \frac{\delta\rho}{\delta z} \frac{1}{(1 + \zeta_z)}. \quad (9)$$

Therefore, a positive wave strain results in a reduction of N^2 and hence, Ri by a factor $1/(1 + \zeta_z)$. Estimated values of ζ_z lead to a 30%–40% reduction in N^2 and the same reduction in Ri; this does not significantly change the dependences shown in Fig. 11.

In estimating ζ_z and ζ_{zz} from the data, we have not distinguished between pure vertical straining and the effects of vertical phase variation. Our results indicate

TABLE 2. Values used to compute the wave stability parameters u/c [Eq. (7)] and Ri_o [Eq. (8)] at depths of 20, 40, and 70 m. Results are plotted in Fig. 11 as a function of phase speed.

z (m)	$\bar{u}$ (m s^{-1})	$\bar{u}_z$ (s^{-1})	N^2 (s^{-2})	ζ (m)	ζ_z	ζ_{zz} (m^{-1})
20	0.0	0.01	.0001	(5–10)	(0.5–1.0)	(0.1–0.2)
40	0.5	0.01	.0002	(5–10)	(0.5–1.0)	(0.1–0.2)
70	0.8	0.0	.0008	(1–3)	(0.1–0.3)	(0.03–0.06)

that between 10 and 40 m there is a consistent phase variation of $\pi/2$ (Fig. 5). Below 40 m there is no phase difference with depth. The effect can be estimated by explicitly including the vertical phase dependence in the depth-dependent function $Z(z)$ introduced in (1); that is,

$$Z(z) = \mathrm{Re}\{|\zeta| e^{i\phi}\} = |\zeta| \cos\phi. \quad (10)$$

Then

$$Z_z = |\zeta|_z \cos\phi - |\zeta| \phi_z \sin\phi, \quad (11)$$

and

$$Z_{zz} = |\zeta|_{zz} \cos\phi - 2|\zeta|_z \phi_z \sin\phi - |\zeta|(\phi_z^2 \cos\phi + \phi_{zz} \sin\phi). \quad (12)$$

Equations (11) and (12) show the wave strain and wave-strain divergence to be comprised of individual terms involving vertical variations of displacement amplitude and vertical variations of phase. The first term on the rhs of (11) represents pure vertical straining, while the second term represents a shearing of the waves interacting with the mean currents. The magnitudes of each of the terms can be evaluated to determine their relative contributions by assigning $\sin\phi$ and $\cos\phi$ both to equal 1. Derivatives of $|\zeta|$ are estimated from Fig. 7, and derivatives of ϕ from Fig. 5. Between 10 m and 40 m, $|\zeta| \sim 5$–10 m; $|\zeta|_z \sim 0.5$ m/30 m $= 0.017$; $|\zeta|_{zz} \sim 0$; $\phi_z \sim (\pi/2)/30$ m ≈ 0.05 rad m^{-1}, $\phi_{zz} \sim 0$. With these estimates, the term $|\zeta|\phi_z$ represents about half of the contribution to our estimate of ζ_z in Table 1, while the terms involving ϕ_z represent a somewhat smaller contribution to Z_{zz}. Consequently, we assume that the wave strain and wave-strain divergence estimated from our data is a combination of both pure vertical straining and shearing.

7. Possible generation mechanisms

Our observations suggest that the combination of a large background shear with surface forcing plays a significant role in generating these waves. Although background values of Ri did not change significantly between day and night or in clear accordance with changes in wind forcing, high-frequency internal waves were observed only at night or in the morning during periods of sustained westward winds. During these periods, a diurnal mixing cycle was also present in the low-Ri thermocline above the EUC core. Events of thermocline mixing occurred almost exclusively in conjunction with the presence of high-wavenumber internal waves.

Our observations appear to be similar to atmospheric observations of convectively forced internal waves by Kuettner et al. (1987). From aircraft observations over the Great Plains, Kuettner et al. (1987) observed internal gravity waves to be ubiquitous at the top of the convectively active boundary layer in the presence of moderate to strong vertical wind shear. Numerical experiments by Clark et al. (1986) and Hauf and Clark (1989) indicated that internal gravity waves forced by convection may in turn be important in organizing convection in the boundary layer. The relationship with turbulence was not addressed, however. A consistent scenario involves generation of internal waves near the surface; the waves then propagate into the low-Ri zone where they quickly dissipate their energy to the mean flow and/or to turbulence. These internal waves could be generated by large-scale mixed-layer eddies impinging on the mixed-layer base and interacting with the mean shear [perhaps similar in nature to the waves produced by the experiments of Thorpe (1984)]. Wijesekera and Dillon (1991) have suggested that this may result in an "obstacle effect," whereby the eddies deform the mixed-layer base; in the presence of shear the deformed mixed-layer base may represent form drag to the flow, analogous to the production of atmospheric lee waves by flow past small hills. This mechanism produces an anisotropic internal wave field with a phase speed approximately that of the average velocity in the mixed layer. If the frequency of the internal waves is near N, the horizontal wavelength would be close to that observed here. Although the equator is a unique environment, it may not be the only location where convectively forced internal waves are formed. In midlatitudes, the base of the mixed layer is frequently a site for enhanced vertical current shear. We suspect that this may also be a site for the generation of phenomena such as observed at the equator, especially at times when the ocean boundary layer is actively convective. In the event that Ri is low as well, the result may be enhanced mixing, as appears to be the case in our equatorial observations.

The other possibility is that the observed features are Kelvin–Helmholz-type instabilities that grow as a consequence of small perturbations introduced to a stratified shear flow at or near critical Ri and would appear as packets of internal waves in our measurements. The horizontal wavelength of these instabilities is $O(2\pi h)$, where h is the thickness of the shear (or density) interface (Turner 1973, p. 99). An estimate of h is obtained from the total change in $\bar{u}$ (or σ_θ) in the low-Ri zone divided by the vertical gradient $\bar{u}_z$ [or $(\sigma_\theta)_z$]; the result is $h \sim 40$ m. The horizontal wavelength, then, is about 250 m, close to the observed peak in the displacement spectrum of Fig. 3. The events that initiate the instabilities must have a diurnal nature and be coupled to the surface forcing. It is possible that the instabilities are triggered by large-scale mixed-layer eddies.

It is probably more likely that the observed wave and turbulence signal is due to a combination of internal waves that have found their way into the low-Ri zone and shear instability that is enhanced by the presence of the waves. Thorpe's (1978) calculations

suggest that the presence of finite-amplitude internal gravity waves in a stratified shear flow will result in a reduction in wave slope for which advective instability occurs. Munk (1981) has suggested that Thorpe's results may also indicate that the presence of internal waves results in an increase of critical *mean* Ri (above 1/4) for which shear instability occurs by increasing the shear and reducing the *instantaneous* Ri below 1/4.

8. Discussion

Coincident measurements of turbulence from a microstructure profiler and high-wavenumber internal waves from a towed thermistor chain indicate a high degree of correlation between mixing and internal waves below the mixed layer in the low-Ri thermocline above the core of the EUC. This supports the notion that mixing in this low-Ri flow is initiated by internal waves. Estimates of turbulent dissipation, vertical isotherm displacement by internal waves, and wave slope were all higher, on average, in the low-Ri zone than elsewhere in the water column. The waves were characteristically intermittent, with active periods of several hours separated by periods of relative calm. The packets of internal waves occurred exclusively at night or in the morning hours and only during the periods of sustained westward winds. The diurnal cycle of mixing in the low-Ri zone was certainly linked to a diurnal cycle in internal wave activity. It is reasonable to assume that the diurnal cycle in turbulent dissipation observed in 1984 (Moum et al. 1989) was also associated with a diurnal cycle in internal wave activity.

The waves exhibited relatively high horizontal wavenumber (corresponding to wavelengths of 150–250 m) and were highly energetic (hourly rms values of vertical displacement were greater than 2 m at least 5% of the time for the first 4 days of our experiment, Fig. 6; peak instantaneous values frequently exceeded 10 m). The consistent phase dependence of the waves with depth probably indicates a dynamical coupling of the waves with the mean flow. If the phase variation was due to passive advection by the mean current, we would have expected the relative phase difference between two depths to be an increasing function of time because of the large shear. Hence, the confidence limits on the averaged phase profile would be much larger than observed. A nonlinear interaction with the mean flow must be acting to maintain the high vertical coherence and tight phase relation exhibited.

The most surprising aspect of our investigations is that it seems that large mixing events in the low-Ri thermocline above the EUC may be due *solely* to breaking internal wave packets. Our results indicate that it is difficult to argue that internal waves are not *the* most important initiator of turbulence in the upper equatorial ocean. The correlation of ϵ with $N^2\langle\zeta^2\rangle$ is high over the full range of measured values of each parameter. The mean value of ϵ was four times greater when waves were present than when they were absent from the low Ri thermocline (Fig. 6). They need only occur a small fraction of the time to dominate the long-term mean dissipation rate, presumably also dominating the mean turbulent fluxes of heat, salt, and momentum. Our combined 1984 and 1987 measurements indicate that the waves were intermittently present on 16 of the 26 nights during which measurements were made. This alters once again our concepts of mixing at the equator. Prior to 1984, our ideas of a steady-state turbulent shear production–turbulent dissipation balance in the stratified shear flow above the EUC followed conventional wisdom. Our 1984 findings of a diurnal cycle in dissipation, which was further modulated by wind stress, demonstrated the impact of short-term variability on the mixing processes and especially in the sampling patterns required to resolve them. Now it seems that the key to mixing in this low-Ri flow may be on yet shorter time scales, and a more intensive investigation focusing on the interactions involving the internal waves is necessary to understand the mixing physics.

The space–time patchiness of the internal wave packets suggests that they do not last very long. Although they seem to be ubiquitous at night (during periods when surface forcing conditions are favorable), they do not appear in the later hours of the daytime. That is, they are generated locally and they dissipate locally. The appropriate time scale for dissipation of internal wave energy by turbulence is $\tau \sim N^2\langle\zeta^2\rangle/\epsilon$, represented by lines of unity slope in Fig. 9. The majority of the points in Fig. 9 are associated with $\tau < 1$ h, which is similar to the observed duration of thermocline bursts during our 1984 time-series measurements. This indicates that the waves cannot propagate very far in the horizontal direction above the EUC core and that absorption of wave energy by the mean flow should be no more than equally as important as turbulence in dissipating the waves. However, the waves may propagate vertically; once below the EUC core, where ϵ is smaller by at least two orders of magnitude, attenuation of wave energy by turbulence should be negligible.

While we have been concentrating on trying to estimate the "small-scale" fluxes of mass and momentum from microstructure measurements at the equator, the dominance of internal waves in the low-Ri zone suggests that we really need to improve our understanding of the effects of the internal waves. Although irreversible mass transport due to the waves may be estimated from the microstructure measurements (since the net effect is due to wave breaking), the momentum transport by the waves must be investigated in other ways. From the 1984 measurements, Dillon et al. (1989) determined that the turbulent momentum transport was insufficient to account for the net imbalance in the zonal momentum budget. They suggested that momentum transport by internal waves may be significant.

Certainly, the frequent occurrence of internal waves during nights coincident with moderate but sustained westward winds suggests that they may be important, at least at some times. On the other hand, Hebert et al. (1991) demonstrated from our 1987 data that an internal wave momentum flux need not be invoked in the zonal momentum budget, the turbulent stress divergence being sufficient. As yet, we cannot determine the contribution of internal waves to the long-term momentum budget.

To summarize, our present view of equatorial mixing is as follows: winds and surface cooling drive mixing in a shallow surface layer (0–15 m); internal waves are generated either by convective forcing, that is, by impingement of surface-layer eddies on the base of the sheared surface layer or by Kelvin–Helmholz-type instabilities; or quite possibly by some combination of these mechanisms. Above the EUC core, our estimates of wave properties from the data and an analysis of plane waves in a shear flow suggest that these waves are inherently unstable to both advective and shear instability mechanisms. As a result, the waves break and generate turbulence. This sequence appears to occur only during periods of sustained westward wind stress.

Acknowledgments. We are grateful to Ayal Anis for a thorough reading of this manuscript and to Hemantha Wijesekera for his insightful comments. Mike Gregg, Murray Levine, Mike McPhaden, and Hartmut Peters also contributed useful comments on this work. This work was funded by the National Science Foundation (OCE-8608256 and OCE-8716719).

APPENDIX

Definitions of Internal Wave Statistics

For comparison of chain and microstructure data, all of our calculations were averaged over 1 hour. Within this period, we collected 6–10 RSVP profiles, 360 10-s-averaged towed thermistor data points (per sensor) and traveled approximately 9 km. For comparison to the towed temperature data, ϵ values were averaged over ±5 m vertically about the mean depth of each thermistor for the 1-h period. Mean values of vertical temperature gradient, T_z, and squared buoyancy frequency, N^2, were computed over matching intervals from the RSVP data.

As a measure of the high-frequency, high-wavenumber internal gravity wave activity, statistics were computed to estimate rms values of wave displacement, ζ; wave potential energy, $N^2\zeta^2$; waveslope, ζ_x; wave strain, ζ_z; and wave strain divergence, ζ_{zz}, from the towed temperature data. We use $\langle \cdot \rangle$ to refer to rms quantities. Our operational definitions for these quantities and the methods used for computing these from the data follow:

T' is the highpass-filtered (periods less than 300 s) temperature record, where T is the 10-s averaged temperature data; $\langle T' \rangle$ is the rms temperature fluctuation due to horizontal scales ranging from 300 s × 2.5 m s^{-1} = 750 m down to 25 m (at 10-s averaging). The upper wavelength was chosen (by examination of spectra; Fig. 3, left panel) to exclude the effects of lateral variability not associated with the apparently narrowband internal gravity wave signal (§4). The lower limit of 25 m is large enough that the influence of turbulent overturns was eliminated from rms estimates.

$\zeta = T'/\overline{T_z}$ is the vertical isotherm displacement due to motions with horizontal scales between 25 and 750 m ($\overline{T_z}$ is the hourly averaged vertical temperature gradient estimated from RSVP data). The rms vertical displacement is $\langle \zeta \rangle = \langle T' \rangle / \overline{T_z}$. Since we feel that most of the nonwave lateral variability (scales > 750 m) and turbulent overturns (scales < 25 m) have been eliminated from the estimate, $\langle \zeta \rangle$ is referred to as rms wave displacement.

$N^2\langle \zeta^2 \rangle$ is the rms wave potential energy, with N^2 obtained from the 1-h averaged RSVP data.

$\langle \zeta_z \rangle$ is the rms value of vertical derivative of the instantaneous isotherm displacement, or wave strain, obtained by computing the average vertical gradient over three adjacent thermistors and assigning this value to the center sensor; $\langle \zeta_{zz} \rangle$ was computed in the same manner from the instantaneous (i.e., 10 s) ζ_z time series. We refer to $\langle \zeta_{zz} \rangle$ as the rms wave-strain divergence.

$\langle \zeta_x \rangle = [\overline{(T_t')^2}]^{1/2}/(U\overline{T_z})$, where the subscript t represents differentiation with respect to time (first difference) and U is the mean ship speed over the interval; $\langle \zeta_x \rangle$ is the rms wave slope.

REFERENCES

Bahr, F. L., and C. A. Paulson, 1991: The effects of rainfall on temperature and salinity in the upper 10 meters of the equatorial Pacific. TOGA Notes, Nova University Press, 9–13.

Baumann, R. J., L. M. deWitt, M. D. Levine, C. A. Paulson, and J. Wagner, 1982: Towed thermistor chain observations across the Gulf Stream. Oregon State University School of Oceanography reference 82-3, 98 pp.

Caldwell, D. R., T. M. Dillon, and J. N. Moum, 1985: The Rapid-Sampling Vertical Profiler: An evaluation. *J. Atmos. Oceanic. Technol.*, **2,** 615–625.

Clark, T. L., T. Hauf, and J. P. Kuettner, 1986: Convectively forced internal gravity waves: Results from two-dimensional numerical experiments. *Quart. J. Roy. Meteor. Soc.*, **112,** 899–925.

deWitt, L. M., R. J. Baumann, C. A. Paulson, T. K. Chereskin, R. M. Samelson, and J. W. Wagner, 1987: Towed thermistor chain observations during Tropic Heat 1987. Oregon State University College of Oceanography reference 87-28, 268 pp.

Dillon, T. M., J. N. Moum, T. K. Chereskin, and D. R. Caldwell, 1989: Zonal momentum balance at the equator. *J. Phys. Oceanogr.*, **19,** 561–570.

Gregg, M. C., H. Peters, J. C. Wesson, N. S. Oakey, and T. J. Shay, 1985: Intensive measurements of turbulence and shear in the Equatorial Undercurrent. *Nature,* **318,** 140–144.

Hauf, T., and T. L. Clark, 1989: Three-dimensional numerical ex-

periments on convectively forced internal gravity waves. *Quart. J. Roy. Meteor. Soc.*, **115,** 309–333.

Hebert, D., J. N. Moum, C. A. Paulson, D. R. Caldwell, T. K. Chereskin, and M. J. McPhaden, 1991: The role of the turbulent stress divergence in the equatorial Pacific zonal momentum balance. *J. Geophys. Res.*, **96,** 7127–7136.

——, ——, ——, and ——, 1992: Turbulence and internal waves at the equator. Part II: Details of a single event. *J. Phys. Oceanogr.*, **22,** 1346–1356.

Jenkins, G. M., and D. G. Watts, 1968: *Spectral Analysis and its Applications.* Holden-Day.

Kuettner, J. P., P. A. Hildebrand, and T. L. Clark, 1987: Convection waves: Observations of gravity wave systems over convectively active boundary layers. *Quart. J. Roy. Meteor. Soc.*, **113,** 445–467.

McPhaden, M. J., and H. Peters, 1992: On the diurnal cycle of internal wave variability in the eastern equatorial Pacific. *J. Phys. Oceanogr.*, **22,** 1317–1329.

Moum, J. N., and D. R. Caldwell, 1985: Local influences on shear flow turbulence in the equatorial ocean. *Science,* **230,** 315–316.

——, ——, and C. A. Paulson, 1989: Mixing in the equatorial surface layer and thermocline. *J. Geophys. Res.*, **94,** 2005–2021.

Munk, W., 1981: Internal waves and small-scale processes. *Evolution of Physical Oceanography,* B. A. Warren and C. Wunsch, Eds., The MIT Press, 264–291.

Peters, H., M. C. Gregg, and J. M. Toole, 1988: On the parameterization of equatorial turbulence. *J. Geophys. Res.*, **93,** 1199–1218.

Thorpe, S. A., 1978: On the shape and breaking of finite amplitude internal gravity waves in a shear flow. *J. Fluid Mech.*, **85,** 7–31.

——, 1984: A laboratory study of stratified accelerating shear flow over a rough boundary. *J. Fluid Mech.*, **138,** 185–196.

Turner, J. S., 1973: *Buoyancy Effects in Fluids.* Cambridge.

Spoering, T. J., 1979: Towed observations of internal waves in the upper ocean. Oregon State University School of Oceanography reference 79-10, 121 pp.

Wijesekera, H., and T. M. Dillon, 1991: Internal waves and mixing in the upper equatorial Pacific ocean. *J. Geophys. Res.*, **96,** 7115–7125.